Journal of Science and Transport Technology
Journal homepage: https://jstt.vn/index.php/en

UNIVERSITY OF TRANSPORT TECHNOLOGY

Nonlinear dynamic responses of functionally graded graphene platelet reinforced composite spherical caps subjected to impulse loads

Nguyen Trong Tam[1], Pham Nhu Nam[2,*], Nguyen Thi Giang[3]
[1]University of Transport Ho Chi Minh City, Ho Chi Minh City, Vietnam
[2]Faculty of Mathematics, Mechanics and Informatics, VNU University of Science, 334 Nguyen Trai Street, Thanh Xuan, Hanoi, Vietnam
[3]Mechanics of Advanced Materials and Structures, University of Transport Technology, Hanoi, Vietnam

Article info
Type of article:
Original research paper

DOI:
https://doi.org/10.58845/jstt.utt.2026.en.6.2.171-186

***Corresponding author:**
Email address:
nampn@utt.edu.vn

Received: 14/10/2025
Received in Revised Form: 24/11/2025
Accepted: 17/12/2025

Abstract: This paper investigates the nonlinear dynamic behavior of functionally graded graphene platelet reinforced composite (FG-GPLRC) shallow axisymmetric spherical caps resting on a nonlinear viscoelastic Pasternak foundation and subjected to transient mechanical loading. The caps are exposed to a thermal environment, yet the mechanical properties of the material are considered temperature-independent. The theoretical framework is established based on higher-order shear deformation theory (HSDT) integrated with von Karman geometric nonlinearity. The governing equations of motion are derived using the Lagrangian approach, incorporating damping effects through the Rayleigh dissipation function. A semi-analytical solution is obtained by combining the Ritz method for spatial discretization and the Runge-Kutta method for time integration. Two forms of impulsive pressure, infinite duration step load and blast load, are examined to evaluate transient responses. Parametric studies are conducted to explore the effects of graphene distribution patterns, mass fraction, geometric parameters, thermal pre-deflection, foundation stiffness, and damping coefficients on the nonlinear response.

Keywords: Impulse load; Step load; Blast load; Nonlinear dynamic response; Euler-Lagrange equation; Rayleigh dissipation function; Higher-order shear deformation theory.

1. Introduction

Circular plates and shallow spherical caps are widely used in engineering applications due to their favorable load-carrying capacity and geometric versatility. While circular plates represent flat structures, spherical caps exhibit inherent curvature, making them more effective in resisting radial pressure and enhancing global stiffness. These components are commonly subjected to both static and dynamic loads, often in conjunction with thermal environments, necessitate advanced modeling approaches for accurate analysis.

Functionally graded materials (FGMs) represent a class of advanced multifunctional composites characterized by the gradual variation of constituent materials through the thickness, enabling tailored control of electro-thermo-mechanical or other engineering requirements. The Kirchhoff plate theory, first-order and higher-order shear deformation theories (FSDT and HSDT) were applied to study the bending analysis of FGM circular plates, applying the axisymmetric deformation assumption by Reddy et al. [1]. Ghomshei [2] analyzed variable-thickness FGM circular plates resting on elastic foundations using FSDT in conjunction with the differential quadrature method. Shariyat and Alipour [3] formulated a semi-analytical power-series-based approach to examine dynamic stresses in sandwich FGM plates. Kiani [4] investigated the dynamic response and vibration characteristics of thermally postbuckled FGM circular plates, highlighting the interplay between thermal fields and geometric nonlinearities. Further contributions include the use of generalized differential quadrature methods [5] and nonlinear Chebyshev-based collocation techniques [6] to explore vibrational behavior under thermal environments. The buckling response of FGM spherical caps has also been addressed in the literature. For instance, thermal and mechanical buckling behavior was examined applying the Donnell–Mushtari–Vlasov theory with simplified Sanders-type kinematics [7], and thermal buckling of deep FGM caps with integrated piezoelectric actuators was analytically studied in [8]. The nonlinear HSDT was applied to study the thermo-mechanical buckling of FGM circular plates and spherical caps using the Ritz energy method [9]. Additionally, by using the variable separation technique, an analytical approach for wave propagation of elastic FGM spherical caps was reported by Qiao et al. [10]. The linear hardening elastoplastic problems for FGM spherical caps were investigated [11] using the closed solutions. The sandwich spherical caps with FGM coatings were considered in the multi-objective optimization for vibration suppression problems [12], using an improved meta-heuristic algorithm. In addition, the stepped spherical-cylindrical shells were considered [13] in dynamic problems using the FSDT and Ritz energy method.

Functionally graded graphene platelet reinforced composites (FG-GPLRCs) are advanced materials formed by embedding graphene platelets (GPLs) within an isotropic matrix according to predefined distribution patterns through the thickness. The exceptional mechanical and multifunctional properties of FG-GPLRCs have made them highly attractive for enhancing the structural performance of a wide variety of plate and shell configurations. Several studies have examined the nonlinear bending, stability, and vibrational responses of FG-GPLRC and porous FG-GPLRC rectangular plates using techniques such as the differential quadrature method [14, 15] and the variational differential quadrature-finite element approach [16]. The natural frequencies of point-supported skew plates made of FG-GPLRCs were analyzed using the first-order shear deformation plate theory (FSDPT) [17], while doubly curved FG-GPLRC sandwich panels subjected to transient loading were modeled with a data-driven computational framework [18]. FG-GPLRC cylindrical shells have also been studied extensively in dynamic response problems [19], including free vibration and buckling analyses [20], as well as thermoelastic bending behavior [21]. Annular plates composed of FG-GPLRCs have been investigated in terms of thermal buckling, vibration, stress distribution, and deformation using FSDPT [22], TSDPT [23], and under complex loading conditions such as magneto-electro-elastic environments [24] or in combination with metal foam cores [25, 26]. Both linear and nonlinear vibrational characteristics of FG-GPLRC circular plates have been addressed using meshfree methods [27] and differential quadrature techniques [28]. Particular attention has been paid to FG-GPLRC spherical caps, where thermal buckling, mechanical buckling, free vibration, and forced vibration problems have been solved via the Ritz energy method [29, 30], Galerkin method [31], and analytical formulations [32].

More recently, Nam et al. [33-36] have contributed to the field of FG-GPLRC spherical caps stiffened with spiderweb and multi-step spiderweb stiffeners by investigating the static and dynamic buckling behavior, employing enhanced smeared stiffener technique and integral partitioning techniques for improved modeling accuracy.

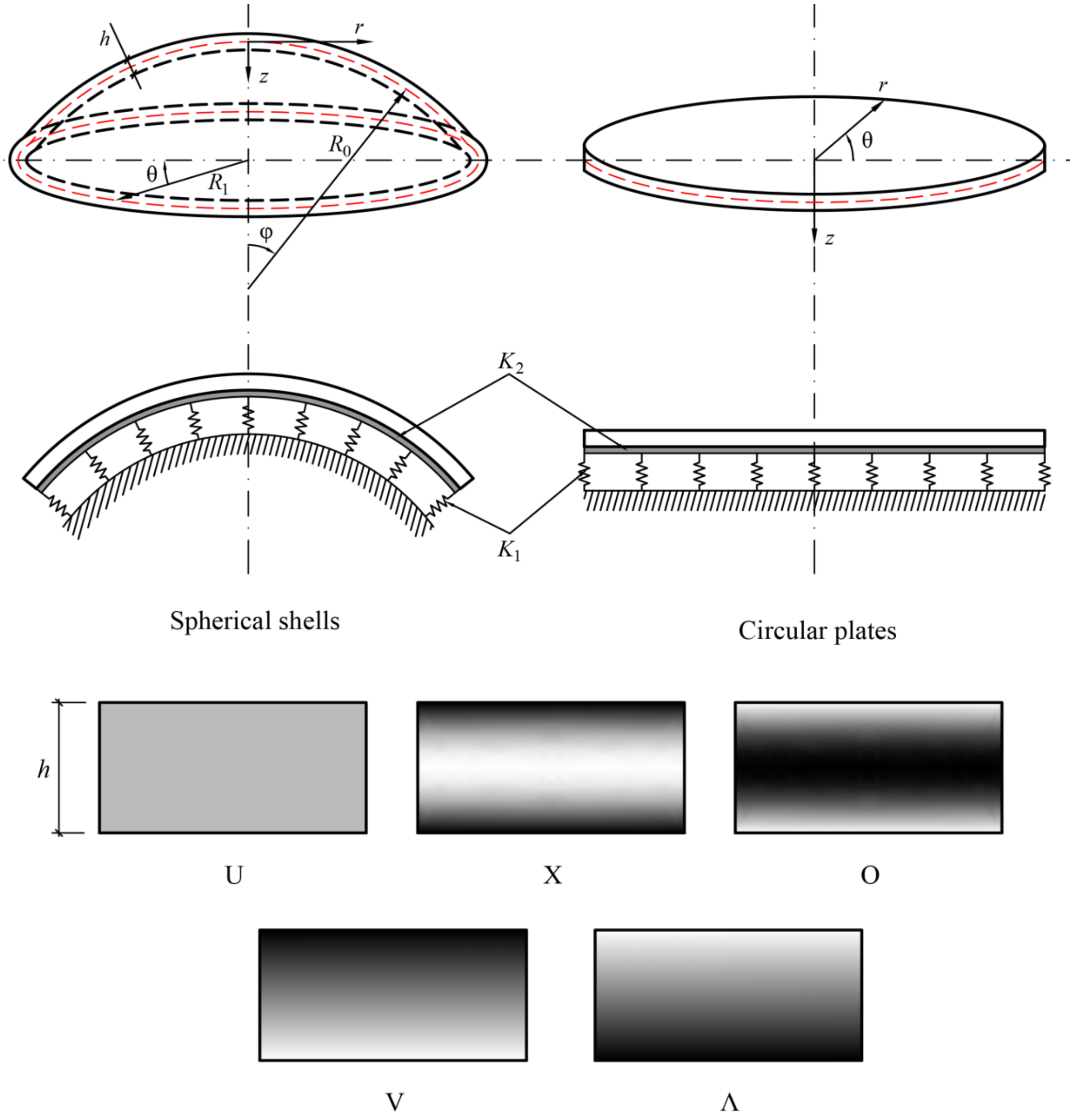

Fig. 1. Coordinate systems and geometric properties of spherical caps, and material distribution laws of FG-GPLRC

From the above discussions, the nonlinear dynamic behavior of FG-GPLRC shallow spherical caps under impulsive loads, particularly with thermal effects and viscoelastic foundation, has not been thoroughly investigated. This gap limits the predictive accuracy for practical applications involving transient loading in curved composite structures. Such loadings are highly relevant in aerospace, defense, and civil engineering applications, where transient external forces may trigger significant dynamic responses and potential instabilities in advanced composite shell structures. Therefore, the present study aims to develop a semi-analytical formulation to determine the nonlinear dynamic responses of axisymmetric spherical caps made from FG-GPLRC subjected to infinite duration step load and blast load. The theoretical framework is based on the HSDT combined with von Karman nonlinearities and viscoelastic foundation modeling. The governing equations are derived using the Lagrangian formulation and solved numerically using the Runge-Kutta method. Through parametric studies, the effects of material gradation, geometrical parameters, impulse characteristics, and foundation stiffness on the nonlinear transient responses are systematically analyzed.

2. FG-GPLRC and spherical caps designs

The spherical caps with shallowness of curvature are considered in this paper (see Fig. 1). By approximating $r = R_0 \sin\varphi$, the exact spherical coordinate system (φ, θ, z) is simplified by the quasi-polar coordinate system (r, θ, z), with the circumferential and meridional directions θ and φ, the main radius R_0, base radius R_1, and centripetal axis z. The caps are considered to be axisymmetric deformations and are placed on the viscoelastic foundation, under time-dependent external pressure q in an environment temperature ΔT.

Five GPL distribution laws, including U, X, O, V, and Λ distributions, are considered in this paper, expressing the GPL mass fraction with respect to the cap thickness $\left(-\frac{h}{2} \le z \le \frac{h}{2}\right)$, as [29-31]

$$W_{GPL}^{*} = \begin{cases} W_{GPL} & \text{U distribution,} \\ \frac{|4z|}{h} W_{GPL} & \text{X distribution,} \\ \left(2 - \frac{4|z|}{h}\right) W_{GPL} & \text{O distribution,} \\ \left(-\frac{2z}{h} + 1\right) W_{GPL} & \text{V distribution,} \\ \left(\frac{2z}{h} + 1\right) W_{GPL} & \Lambda \text{ distribution,} \end{cases} \tag{1}$$

where total GPL mass fraction is defined by W_{GPL}.

The GPL volume fraction is defined as

$$V_{GPL} = \frac{\rho_m W_{GPL}^{*}}{\rho_m W_{GPL} + \rho_{GPL}\left(1 - W_{GPL}\right)}, \tag{2}$$

where the GPL volume fraction is denoted by V, ρ is the denote of density; matrix and GPL are respectively denoted by the subscripts m and GPL ; and note that $V_m + V_{GPL} = 1$.

Based on the Halpin-Tsai model, the elastic modulus is estimated by

$$\bar{E} = \frac{3E_m + 3E_m\Theta_1 V_{GPL}\Gamma_1}{8 - 8V_{GPL}\Gamma_1} + \frac{5E_m + 5E_m\Theta_2 V_{GPL}\Gamma_2}{8 - 8V_{GPL}\Gamma_2}, \tag{3}$$

where

$$\Gamma_1 = \frac{-E_m + E_{GPL}}{E_{GPL} + E_m\Theta_1}, \; \Gamma_2 = \frac{-E_m + E_{GPL}}{E_{GPL} + E_m\Theta_2}, \quad \Theta_1 = \frac{2a_{GPL}}{t_{GPL}}, \; \Theta_2 = \frac{2b_{GPL}}{t_{GPL}}, \tag{4}$$

with the GPL length, width, and thickness are denoted by a_{GPL}, b_{GPL}, and t_{GPL}; the elastic modulus is denoted by E.

By using the mixture rule, the Poisson ratio, thermal expansion coefficient, and density ($\bar{\nu}$, $\bar{\alpha}$, and $\bar{\rho}$), with respect to the cap thickness, are obtained by

$$\begin{aligned} \bar{\nu} &= \nu_m V_m + \nu_{GPL} V_{GPL}, \\ \bar{\alpha} &= \alpha_m V_m + \alpha_{GPL} V_{GPL}, \\ \bar{\rho} &= \rho_m V_m + \rho_{GPL} V_{GPL}. \end{aligned} \tag{5}$$

The thermal stresses are counted in the formulations as the pre-stresses and combined with Hookian law, obtained as

$$\begin{Bmatrix} \sigma_r \\ \sigma_\theta \end{Bmatrix} = \begin{bmatrix} \bar{Q}_{11} & \bar{Q}_{12} \\ \bar{Q}_{12} & \bar{Q}_{22} \end{bmatrix} \left\{ \begin{bmatrix} \varepsilon_r \\ \varepsilon_\theta \end{bmatrix} - \begin{bmatrix} \bar{\alpha} \\ \bar{\alpha} \end{bmatrix} \Delta T \right\}, \quad \sigma_{rz} = \bar{Q}_{44}\varepsilon_{rz}, \tag{6}$$

where the reduced stiffnesses are presented by

$$\bar{Q}_{11} = \bar{Q}_{22} = \frac{\bar{E}}{1 - \bar{\nu}^2}, \; \bar{Q}_{12} = \frac{\bar{E}\bar{\nu}}{1 - \bar{\nu}^2}, \quad \bar{Q}_{44} = \frac{\bar{E}}{2 + 2\bar{\nu}}. \tag{7}$$

The displacements at a distance z from the mid-surface are established by applying the HSDT, taking into account the axisymmetric deformations, presented as

$$\begin{Bmatrix} \bar{u} \\ \bar{v} \\ \bar{w} \end{Bmatrix} = \begin{Bmatrix} u(r) - \dfrac{4z^3}{3h^2}\left[\phi(r) + w(r)_{,r}\right] + \phi(r)z \\ 0 \\ w^*(r) + w(r) \end{Bmatrix}, \tag{8}$$

where $\bar{u} = \bar{u}(r,z)$, $\bar{v} = \bar{v}(r,z)$, and $\bar{w} = \bar{w}(r,z)$ are the displacements; $\phi(r)$ is the rotation, and imperfect deflection $w^*(r)$ is also considered.

The strain expressions at a distance z from the mid-surface can be presented by

$$\begin{Bmatrix} \varepsilon_r \\ \varepsilon_\theta \\ \varepsilon_{rz} \end{Bmatrix} = \begin{Bmatrix} \varepsilon_r^{(0)} \\ \varepsilon_\theta^{(0)} \\ \varepsilon_{rz}^{(0)} \end{Bmatrix} + z\begin{Bmatrix} \phi_{,r} \\ \dfrac{\phi}{r} \\ 0 \end{Bmatrix} - z^2\begin{Bmatrix} 0 \\ 0 \\ \dfrac{4}{3h^2}\left(\phi + w_{,r}\right) \end{Bmatrix} - z^3\begin{Bmatrix} \dfrac{4}{3h^2}\left(\phi_{,r} + w_{,rr}\right) \\ \dfrac{4}{3h^2}\left(\dfrac{\phi}{r} + \dfrac{1}{r}w_{,r}\right) \\ 0 \end{Bmatrix}. \tag{9}$$

The mid-surface strains $\varepsilon_r^{(0)}, \varepsilon_\theta^{(0)}, \varepsilon_{rz}^{(0)}$ considering the von Karman nonlinearities, are derived by

$$\begin{Bmatrix} \varepsilon_r^{(0)} \\ \varepsilon_\theta^{(0)} \\ \varepsilon_{rz}^{(0)} \end{Bmatrix} = \begin{Bmatrix} \dfrac{1}{2}w_{,r}^2 - \dfrac{w}{R_0} + u_{,r} + w_{,r}w_{,r}^* \\ \dfrac{u}{r} - \dfrac{w}{R_0} \\ w_{,r} + \phi \end{Bmatrix}. \tag{10}$$

In the present paper, the governing relations are initially formulated for shallow spherical caps, and the corresponding expressions for circular plates can be derived as a special case by allowing the main radius to approach infinity. The expressions of force, shear resultants, and bending moments associated with axisymmetric deformation are obtained through the integration of the generalized Hookian constitutive equations, presented as

$$\begin{Bmatrix} N_r \\ N_\theta \\ M_r \\ M_\theta \\ P_r \\ P_\theta \end{Bmatrix} = \begin{Bmatrix} \bar{B}_{11} & \bar{B}_{12} & \bar{C}_{11} & \bar{C}_{12} & \bar{D}_{11} & \bar{D}_{12} \\ \bar{B}_{12} & \bar{B}_{22} & \bar{C}_{12} & \bar{C}_{22} & \bar{D}_{12} & \bar{D}_{22} \\ \bar{C}_{11} & \bar{C}_{12} & \bar{F}_{11} & \bar{F}_{12} & \bar{G}_{11} & \bar{G}_{12} \\ \bar{C}_{12} & \bar{C}_{22} & \bar{F}_{12} & \bar{F}_{22} & \bar{G}_{12} & \bar{G}_{22} \\ \bar{D}_{11} & \bar{D}_{12} & \bar{G}_{11} & \bar{G}_{12} & \bar{H}_{11} & \bar{H}_{12} \\ \bar{D}_{12} & \bar{D}_{22} & \bar{G}_{12} & \bar{G}_{22} & \bar{H}_{12} & \bar{H}_{22} \end{Bmatrix} \begin{Bmatrix} \varepsilon_r^{(0)} \\ \varepsilon_\theta^{(0)} \\ \phi_{,r} \\ \dfrac{\phi}{r} \\ -\dfrac{4}{3h^2}\left(\phi_{,r} + w_{,rr}\right) \\ -\dfrac{4}{3h^2}\left(\dfrac{\phi}{r} + \dfrac{1}{r}w_{,r}\right) \end{Bmatrix} - \begin{Bmatrix} \bar{\Phi}_1 \\ \bar{\Phi}_1 \\ \bar{\Phi}_2 \\ \bar{\Phi}_2 \\ \bar{\Phi}_3 \\ \bar{\Phi}_3 \end{Bmatrix}\Delta T, \begin{Bmatrix} Q_r \\ R_r \end{Bmatrix} = \begin{Bmatrix} \bar{I}_{44} & \bar{I}_{45} \\ \bar{I}_{45} & \bar{I}_{55} \end{Bmatrix} \begin{Bmatrix} \varepsilon_{rz}^{(0)} \\ -\dfrac{4}{3h^2}\left(\phi + w_{,r}\right) \end{Bmatrix}, \tag{11}$$

where

$$\left(\bar{B}_{ij}, \bar{C}_{ij}, \bar{F}_{ij}, \bar{D}_{ij}, \bar{G}_{ij}, \bar{H}_{ij}\right) = \int_{-h/2}^{h/2} \bar{Q}_{ij}\left(1, z, z^2, z^3, z^4, z^6\right)dz,$$

$(\ ij = 1,\ 2\ )$,

$$\left(\bar{I}_{44}, \bar{I}_{45}, \bar{I}_{55}\right) = \int_{-h/2}^{h/2} \bar{Q}_{44}\left(1, z^2, z^4\right)dz,$$

$$\left(\bar{\Phi}_1, \bar{\Phi}_2, \bar{\Phi}_3\right) = \int_{-h/2}^{h/2} \left(\bar{Q}_{11} + \bar{Q}_{12}\right)\bar{\alpha}\left(1, z, z^3\right)dz.$$

Taking into account the reaction forces from the Pasternak-type foundation, the strain energy of the structure, the external work, and the kinematic energy, while incorporating the nonlinear characteristics of the foundation, can be respectively formulated as

$$\bar{U}_{int} = \pi \times \int_{-h/2}^{h/2}\int_0^{R_1}\left[\sigma_r\varepsilon_r - \sigma_r\bar{\alpha}\Delta T + \sigma_\theta\varepsilon_\theta - \sigma_\theta\bar{\alpha}\Delta T + \sigma_{rz}\varepsilon_{rz}\right]rdrdz, \tag{12}$$

$$\bar{U}_{ext} = 2\pi\int_0^{R_1} qwrdr - \pi\int_0^{R_1}\left\{\left[K_1 w - K_2\left(w_{,rr} + \frac{1}{r}w_{,r}\right)\right]w\right\}rdr, \tag{13}$$

$$\bar{U}_T = \pi\int_{-h/2}^{h/2}\int_0^{R_1}\bar{\rho}\bar{w}_{,t}^2 rdrdz, \tag{14}$$

where the linear Winkler and Pasternak stiffnesses are respectively denoted by K_1(N/m^3) and K_2 (N/m).

The total potential energy is established from Eqs. (12), (13), and (14), as

$$\bar{U} = \bar{U}_T - \bar{U}_{int} + \bar{U}_{ext}. \tag{15}$$

3. Approximate Solutions and Dynamic Analysis

The structures are assumed to satisfy axisymmetric, clamped, and immovable boundary conditions, which are mathematically imposed as

$$\begin{aligned} &\text{At } r = 0: \quad u = 0,\ \phi = 0,\ w_{,r} = 0,\ w = \text{finite}, \\ &\text{At } r = R_1: \ w = 0,\ w_{,r} = 0,\ \phi = 0,\ u = 0. \end{aligned} \tag{16}$$

The admissible displacement fields that fulfill the prescribed boundary conditions are assumed to take the following forms [9]

$$\begin{aligned} &u = Ur\frac{\left(-r + R_1\right)}{R_1^2}, \quad \phi = \Phi r\frac{\left(-r^2 + R_1^2\right)}{R_1^3}, \\ &w = W\frac{\left(-r^2 + R_1^2\right)^2}{R_1^4},\ w^* = \kappa h\frac{\left(-r^2 + R_1^2\right)^2}{R_1^4}, \end{aligned} \tag{17}$$

where the imperfection w^* is assumed to be similar form to deflection, and κ is the imperfection size.

To incorporate the damping behavior of the foundation, the Rayleigh dissipation function is introduced and integrated into the formulation through the application of the Euler–Lagrange equations, as follows

$$\begin{aligned} &\frac{d}{dt}\left(\frac{\partial \bar{U}}{\partial \dot{W}}\right) - \frac{\partial \bar{U}}{\partial W} + \frac{\partial d_1}{\partial \dot{W}} = 0, \\ &\frac{d}{dt}\left(\frac{\partial \bar{U}}{\partial \dot{U}}\right) - \frac{\partial \bar{U}}{\partial U} = 0, \\ &\frac{d}{dt}\left(\frac{\partial \bar{U}}{\partial \dot{\Phi}}\right) - \frac{\partial \bar{U}}{\partial \Phi} = 0, \end{aligned} \tag{18}$$

where the viscous potential function is

$$d_1 = \pi \int_0^{R_1} c\dot{w}^2 r dr.$$

By substituting Eq. (17) into the expression for the total potential energy given in Eq. (15), and subsequently incorporating the result into Eq. (18), the governing equations of motion can be derived as

$$\bar{b}_{11}U + \bar{b}_{12}\Phi + \bar{b}_{13}W + \bar{b}_{14}W\left(W + 2\kappa h\right) = 0, \tag{19}$$

$$\bar{b}_{12}U + \bar{b}_{22}\Phi + \bar{b}_{23}W + \bar{b}_{24}W\left(W + 2\kappa h\right) = 0, \tag{20}$$

$$\begin{aligned} &\bar{b}_{31}U + \bar{b}_{32}\Phi + \bar{b}_{33}U\left(W + \kappa h\right) + \bar{b}_{34}\Phi\left(W + \kappa h\right) \\ &+ \bar{b}_{35}W\left(W + 4\kappa h/3\right) \\ &+ \bar{b}_{36}W\left(W + \kappa h\right)\left(W + 2\kappa h\right) \\ &+ \bar{b}_{38}W + \bar{b}_{39}\Delta T\left(W + \kappa h\right) \\ &+ \bar{b}_{310}\Delta T + \bar{b}_{311}q - \pi R_1^2\left(c\dot{W} + \bar{b}_{312}\ddot{W}\right)/5 = 0, \end{aligned} \tag{21}$$

where

$$\bar{b}_{11} = -\frac{\pi}{6}\left(\bar{B}_{22} + 2\bar{B}_{11}\right),$$

$$\bar{b}_{12} = \frac{\pi}{60}\left[\frac{4}{3h^2}\left(14\bar{D}_{22} + 34\bar{D}_{11}\right) - 14\bar{C}_{22} - 34\bar{C}_{11}\right],$$

$$\begin{aligned} \bar{b}_{13} = &-\frac{4}{3h^2}\frac{\pi}{15R_1}\left(34\bar{D}_{11} + 14\bar{D}_{22}\right) \\ &+ \frac{\pi R_1}{R_0}\left(3\bar{B}_{11} + 19\bar{B}_{22} + 22\bar{B}_{12}\right), \end{aligned}$$

$$\bar{b}_{14} = \frac{\pi}{315R_1}\left(46\bar{B}_{11} - 82\bar{B}_{12}\right),$$

$$\begin{aligned} \bar{b}_{22} = \frac{\pi}{12}\Bigg[&\frac{4}{3h^2}\left(24\bar{G}_{11} + 6I_{45}R_1^2 + 8\bar{G}_{22}\right) - \left(\frac{4}{3h^2}\right)^2 \\ &\times\left(12\bar{H}_{11} + 9R_1^2\bar{I}_{55} + 4\bar{H}_{22}\right) + \bar{I}_{44}R_1^2 + 4\bar{F}_{22} + 12\bar{F}_{11}\Bigg], \end{aligned}$$

$$\begin{aligned} \bar{b}_{23} = &\frac{\pi\left[\left(3\bar{I}_{55}R_1^2 + 4\bar{H}_{22}/3 + 4\bar{H}_{11}\right)\left(\frac{4}{3h^2}\right)^2\right]}{R_1} \\ &+ \frac{\pi\left[\frac{R_1^2\bar{I}_{44}}{3} - \left(4\bar{G}_{11} + 2\bar{I}_{45}R_1^2 + 4\bar{G}_{22}/3\right)\frac{4}{3h^2}\right]}{R_1} \\ &- \frac{\pi R_1\left[\left(\bar{D}_{22} + \bar{D}_{11}/3 + 4\bar{D}_{12}/3\right)\right]}{3h^2R_0} \\ &+ \frac{\pi R_1\left[2\bar{C}_{22} + 8\bar{C}_{12}/3 + 2\bar{C}_{11}/3\right]}{8R_0}, \end{aligned}$$

$$\bar{b}_{24} = -\frac{\pi\left[\left(2\bar{D}_{11}/3 - 2\bar{D}_{12}\right)\frac{4}{3h^2} + 2\bar{C}_{12} - 2\bar{C}_{11}/3\right]}{5R_1},$$

$$\bar{b}_{31}=\frac{\pi R_1\left(19\bar{B}_{22}+22\bar{B}_{12}+3\bar{B}_{11}\right)}{105R_0}$$
$$-\frac{4\pi\left(14\bar{D}_{22}+34\bar{D}_{11}\right)/3h^2}{15R_1},$$

$$\bar{b}_{33}=\frac{2\pi\left(-82\bar{B}_{12}+46\bar{B}_{11}\right)}{315R_1},$$

$$\bar{b}_{34}=\frac{2\pi\left[\left(-2\bar{D}_{11}+6\bar{D}_{12}\right)\frac{4}{3h^2}+2\bar{C}_{11}-6\bar{C}_{12}\right]}{15R_1},$$

$$\bar{b}_{32}=-\frac{\pi\left[\left(-3R_1^2\bar{I}_{55}-4\bar{H}_{22}/3-4\bar{H}_{11}\right)\left(\frac{4}{3h^2}\right)^2\right]}{R_1}$$
$$-\frac{\pi\left[-\frac{\bar{I}_{44}R_1^2}{3}+\left(2\bar{I}_{45}R_1^2+4\bar{G}_{22}/3+4\bar{G}_{11}\right)\frac{4}{3h^2}\right]}{R_1}$$
$$-\frac{\pi R_1\left[\frac{8}{3h^2}\left(\bar{D}_{11}/3+4\bar{D}_{12}/3+2\bar{D}_{22}\right)\right]}{8R_0}$$
$$-\frac{\pi R_1\left[-2\bar{C}_{22}-2\bar{C}_{11}/3-8\bar{C}_{12}/3\right]}{8R_0},$$

$$\bar{b}_{35}=\frac{4}{3h^2}\frac{4\pi\left(2\bar{D}_{11}-6\bar{D}_{12}\right)}{5R_1^2}+\frac{4\pi\left(\bar{B}_{11}+\bar{B}_{12}\right)}{5R_0},$$

$$\bar{b}_{36}=-\pi\frac{128\bar{B}_{11}}{105R_1^2},\bar{b}_{39}=\frac{4}{3}\pi\bar{\Phi}_1,$$

$$\bar{b}_{310}=-\frac{2R_1^2\pi\bar{\Phi}_1}{3R_0},\bar{b}_{311}=\frac{\pi}{3}R_1^2,\bar{b}_{312}=\int_{-h/2}^{h/2}\bar{\rho}dz.$$

$$\bar{b}_{38}=\frac{\pi\left[-R_1^4K_1/20-4\left(\frac{4}{3h^2}\right)^2\left(\bar{H}_{11}+\frac{\bar{H}_{22}}{3}\right)\right]}{4R_1^2}$$
$$+\frac{\pi R_1^2\left[2\bar{I}_{45}\frac{4}{3h^2}-\frac{K_2}{3}-3\left(\frac{4}{3h^2}\right)^2\bar{I}_{55}-\frac{\bar{I}_{44}}{3}\right]}{4R_1^2}$$
$$+\frac{8\pi\left(\bar{D}_{11}+3\bar{D}_{22}+4\bar{D}_{12}\right)}{9h^2R_0}-\frac{R_1^2\pi\left(\bar{B}_{11}+\bar{B}_{22}+2\bar{B}_{12}\right)}{5R_0^2},$$

Solving Eqs. (19) and (20) to obtain the amplitudes U and Φ, then, substituting them into Eq. (21), presented by

$$\begin{gathered}\left(\bar{c}_{11}\bar{b}_{31}+\bar{b}_{38}+\bar{c}_{21}\bar{b}_{32}\right)W\\+\left(\bar{c}_{21}\bar{b}_{34}+\bar{c}_{11}\bar{b}_{33}\right)W\left(h\kappa+W\right)\\+\left(\bar{c}_{22}\bar{b}_{32}+\bar{c}_{12}\bar{b}_{31}\right)W\left(2\kappa h+W\right)\\+\bar{b}_{35}W\left(W+4\kappa h/3\right)\\+\left(\bar{c}_{22}\bar{b}_{34}+\bar{b}_{36}+\bar{c}_{12}\bar{b}_{33}\right)W\left(2\kappa h+W\right)\left(\kappa h+W\right)\\+\bar{b}_{39}\Delta T\left(h\kappa+W\right)+\Delta T\bar{b}_{310}+q\bar{b}_{311}\\=\frac{\pi R_1^2}{5}\left(\bar{b}_{312}\ddot{W}+c\dot{W}\right),\end{gathered}\tag{22}$$

where

$$\bar{c}_{11}=\frac{\bar{b}_{12}\bar{b}_{23}-\bar{b}_{13}\bar{b}_{22}}{\bar{b}_{11}\bar{b}_{22}-\bar{b}_{12}^2},\bar{c}_{12}=\frac{\bar{b}_{12}\bar{b}_{24}-\bar{b}_{14}\bar{b}_{22}}{\bar{b}_{11}\bar{b}_{22}-\bar{b}_{12}^2},$$
$$\bar{c}_{21}=\frac{\bar{b}_{12}\bar{b}_{13}-\bar{b}_{11}\bar{b}_{23}}{\bar{b}_{11}\bar{b}_{22}-\bar{b}_{12}^2},\ \bar{c}_{22}=\frac{\bar{b}_{12}\bar{b}_{14}-\bar{b}_{11}b_{24}}{\bar{b}_{11}\bar{b}_{22}-\bar{b}_{12}^2}.$$

In the case of free vibration, the linearized form of the governing equation is derived by omitting the geometric nonlinear terms, viscous damping effects, and external forcing. Under these simplifications, the resulting equation of motion describes undamped, unforced vibration, from which the expression for the fundamental frequency is determined as follows

$$\omega=\sqrt{-\frac{5\left(\bar{c}_{11}\bar{b}_{31}+\bar{c}_{21}\bar{b}_{32}+\Delta T\bar{b}_{39}+\bar{b}_{38}\right)}{\bar{b}_{312}\pi R_1^2}}.\tag{23}$$

Two types of time-dependent impulse loads are investigated in the numerical investigations, including blast load and step load, which are respectively defined as

for blast load

$$q(t)=\begin{cases}Q\left(1-\frac{t}{T}\right), & 0\le t\le T\\0, & t>T\end{cases}\tag{24}$$

and for step load

$$q(t)=\begin{cases}Q, & 0\le t\le T\\0, & t>T\end{cases}\tag{25}$$

where the vibration period is denoted by $T=\frac{2\pi}{\omega}$.

The time-dependent laws of impulse loads are applied and substituted into the motion equation (22), and then the resultant is solved using the Runge-Kutta method.

4. Numerical examples

Table 1 presents the comparison of the dimensionless fundamental frequencies of FG-GPLRC circular plates obtained from the present semi-analytical formulation with those reported by Chien and Phuc [27] and Javani et al. [28], which were based on meshfree and differential quadrature methods, respectively. The results are shown for three typical GPL distributions (U, X, and O types) under identical geometrical and material conditions. It can be observed that the present results show excellent agreement with the previous studies, thereby confirming the validity and accuracy of the proposed approach.

In this paper, the material properties of FG-GPLRC are assumed to be temperature-independent and are applied by referring to the previous works [33-35].

Table 1. Validations of non-dimensional fundamental frequencies $\bar{\omega} = \omega R_1^2 \sqrt{\rho_m h/\Pi_m}$ of FG-GPLRC circular plates (W_{GPL} =1%, E_m =3GPa, ρ_m =1200kg/m^3, ν_m =0.34, R_1 =1m, $\Pi_m = E_m h^3 / 12\left(1-\nu_m{}^2\right)$)

Distributions	References	R_1/h		
		5	10	29.4118
U	Chien and Phuc [27]	19.0329	20.5657	21.2205
	Javani et al. [28]	19.1378	20.6418	21.1638
	Present	19.6549	20.9684	21.4086
X	Chien and Phuc [27]	20.6648	23.1168	24.1789
	Javani et al. [28]	21.7190	23.9322	24.7333
	Present	21.6710	24.1887	25.1197
O	Chien and Phuc [27]	16.3881	17.3051	17.7029
	Javani et al. [28]	15.7053	16.5524	16.8334
	Present	16.0492	16.6377	16.8242

Table 2 reports the fundamental frequencies of FG-GPLRC shallow spherical caps and circular plates with various graphene platelet (GPL) distribution types (U, X, V, Λ, and O) and GPL mass fractions ranging from 0% to 0.8%. Several key trends can be observed from the data. First, for both circular plates and spherical caps, an increase in the GPL mass fraction leads to a noticeable rise in the fundamental frequency, confirming the stiffening effect of GPLs on the structure. This effect is particularly prominent in the X-type distribution, where GPLs are concentrated near the top and bottom surfaces. For instance, when the mass fraction increases from 0% to 0.8%, the frequency of the X-type spherical cap rises from 1647.1 rad/s to 2141.9 rad/s, which represents a substantial enhancement in stiffness. Second, among all the distribution types, the X-type configuration consistently exhibits the highest frequencies, followed by V and Λ types, while the O-type produces the lowest. This order corresponds to the relative efficiency of GPL placement across the thickness: surface-concentrated reinforcement (X-type) is more effective in increasing bending rigidity than center-concentrated or uniformly distributed configurations. Third, spherical caps demonstrate significantly higher fundamental frequencies compared to their corresponding circular plates under identical material and geometrical parameters. This increase is due to the inherent geometric curvature of spherical caps, which provides additional stiffness and resistance to deformation.

Table 2. Fundamental frequencies of FG-GPLRC spherical caps and circular plates with various GPL distributions and mass fractions (rad/s, $h = 0.02\text{m}$, $R_1 = 20h$, $R_0 = R_1/0.1$, $\kappa = 0$, $\Delta T = 100\text{K}$, $K_1 = 10$ MN/m^3, $K_2 = 0.1$ MN/m)

	W_{GPL}	U	X	V	Λ	O
Circular plates	0%	879.3	879.3	879.3	879.3	879.3
	0.2%	941.3	1003.5	936.8	936.8	874.4
	0.4%	1001.7	1113.6	986.4	986.4	874.0
	0.6%	1060.5	1213.5	1031.3	1031.3	877.7
	0.8%	1117.9	1305.4	1073.1	1073.1	885.1
Spherical caps	0%	1647.1	1647.1	1647.1	1647.1	1647.1
	0.2%	1751.8	1785.6	1747.8	1750.1	1716.3
	0.4%	1851.4	1912.9	1839.4	1844.1	1784.0
	0.6%	1946.7	2031.1	1924.3	1931.3	1850.2
	0.8%	2038.1	2141.9	2004.1	2013.4	1914.9

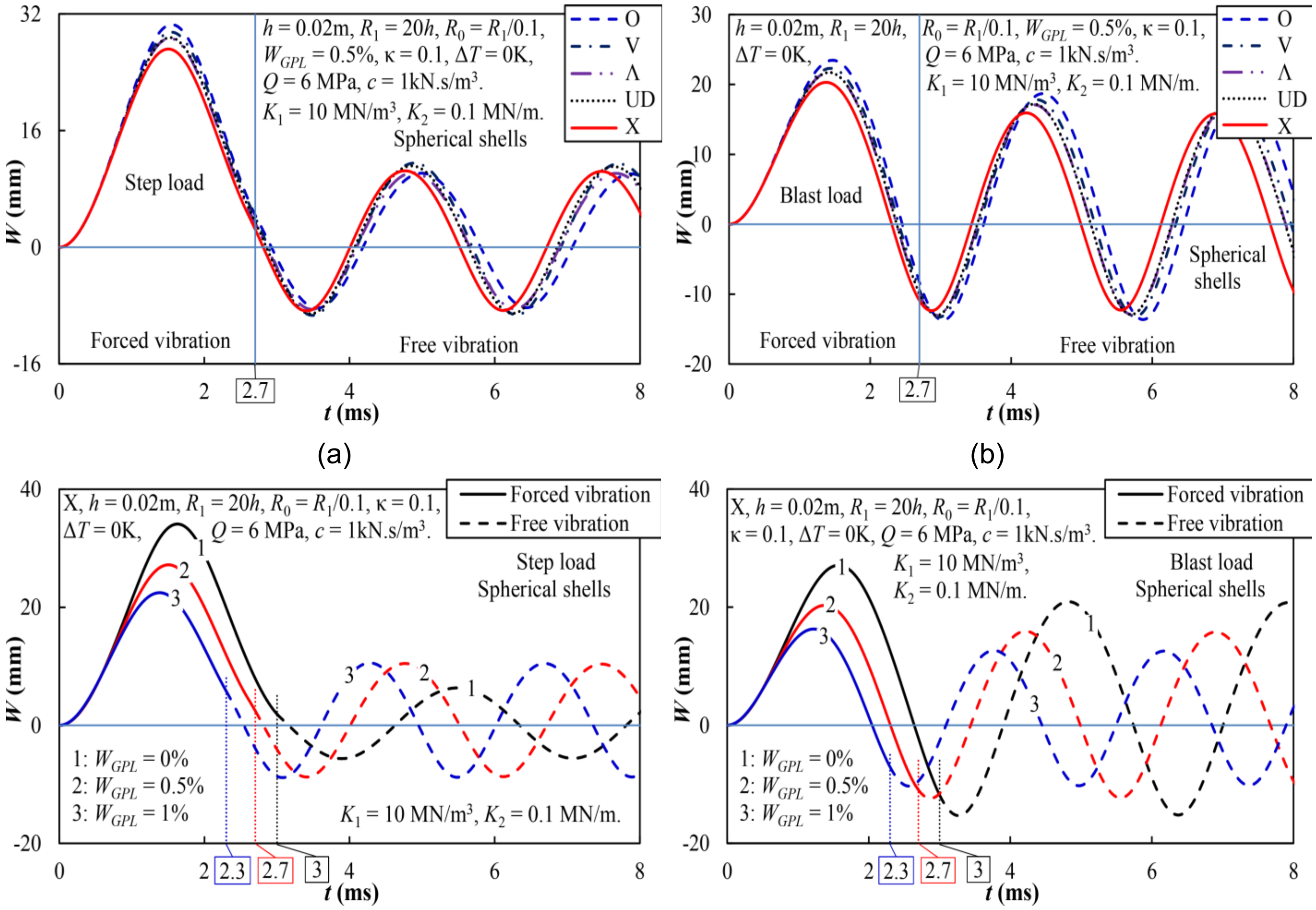

(a) (b)

(c) (d)

Fig. 2. Effects of GPL distribution laws and GPL mass fraction on the dynamic responses of FG-GPLRC spherical caps under impulse loads

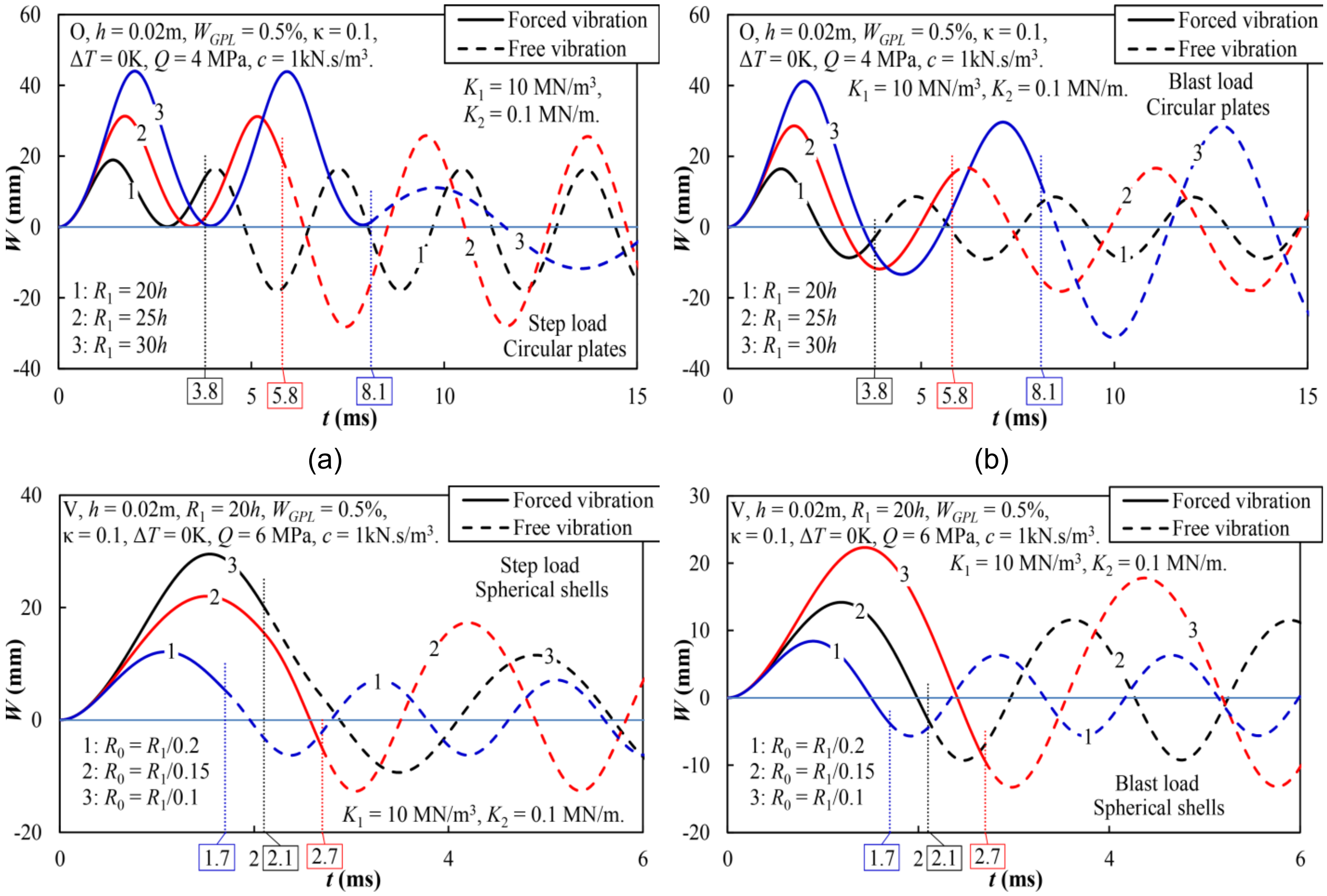

(a) (b)

(c) (d)

Fig. 3. Effects of geometrical properties on the dynamic responses of FG-GPLRC spherical caps under impulse loads

Fig. 2 illustrates the dynamic responses of FG-GPLRC spherical caps under two types of impulse loads, step load and blast load, considering different GPL distribution types (a, b) and various GPL mass fractions (c, d). Figs. 2a and 2b compare the effects of five typical GPL distribution types (U, X, V, Λ, and O) under step and blast loads, respectively. In both loading scenarios, the X-type distribution leads to the lowest deflection amplitudes, indicating the most favorable structural performance. This is due to the reinforcement being concentrated near the outer surfaces of the shell, where bending stiffness is most critical. Conversely, the O-type distribution consistently yields the largest deflections, as the GPLs are primarily concentrated near the mid-surface, which contributes less effectively to flexural rigidity. This confirms that not only the amount of reinforcement but also its through-thickness distribution significantly affects the dynamic behavior under impulsive excitations. Figs. 2c and 2d present the effect of increasing GPL mass fractions under step and blast loading conditions. A clear trend is observed: as the GPL content increases from 0% to 1%, the peak deflection of the spherical cap decreases noticeably with the loading duration. This reflects the expected stiffening effect of GPLs, which enhances the resistance of the structure to transient loads. Moreover, the reduction in displacement is more pronounced under step loading (Fig. 2c). In the case of step loading, irregularities in the order of vibration amplitudes among different GPL mass fractions can be observed after the load duration, when the structure is no longer subjected to external excitation.

Fig. 3 investigates the influence of geometrical parameters, specifically the base radius R_1 and the main (curvature) radius R_0, on the nonlinear dynamic responses of FG-GPLRC spherical caps under step and blast impulse loads. Figs. 3a and 3b illustrate the effects of increasing base radius R_1 under step and blast loads, respectively. It is observed that as R_1 increases, the peak displacement of the cap also increases, indicating a reduction in structural stiffness. Figs. 3c and 3d explore the effects of varying the main radius R_0, which governs the global curvature of the cap. A larger value of R_0 implies a shallower curvature, approaching a flat plate as $R_0 \to \infty$. The results show that increasing R_0 leads to increased dynamic deflection, consistent with the notion that deeper caps (smaller R_0) exhibit greater geometric stiffness.

Fig. 4 examines the effects of environmental temperature on the dynamic responses of FG-GPLRC spherical caps subjected to step (Fig. 4a) and blast (Fig. 4b) impulse loads. In this study, the mechanical properties of the FG-GPLRC material are assumed to be temperature-independent. Therefore, the variations in structural response are attributed solely to the thermal expansion-induced pre-deformation of the structure, rather than material degradation. As the temperature increases, a thermal expansion field is induced in the spherical cap, generating initial deflection in the negative direction of the axial coordinate z. This pre-buckling deformation causes the dynamic displacement response to shift toward the negative domain, as clearly observed in both figures. Notably, this shift does not imply an increase in vibration amplitude, but rather a relocation of the mean position of oscillation due to the thermally-induced geometric deformation.

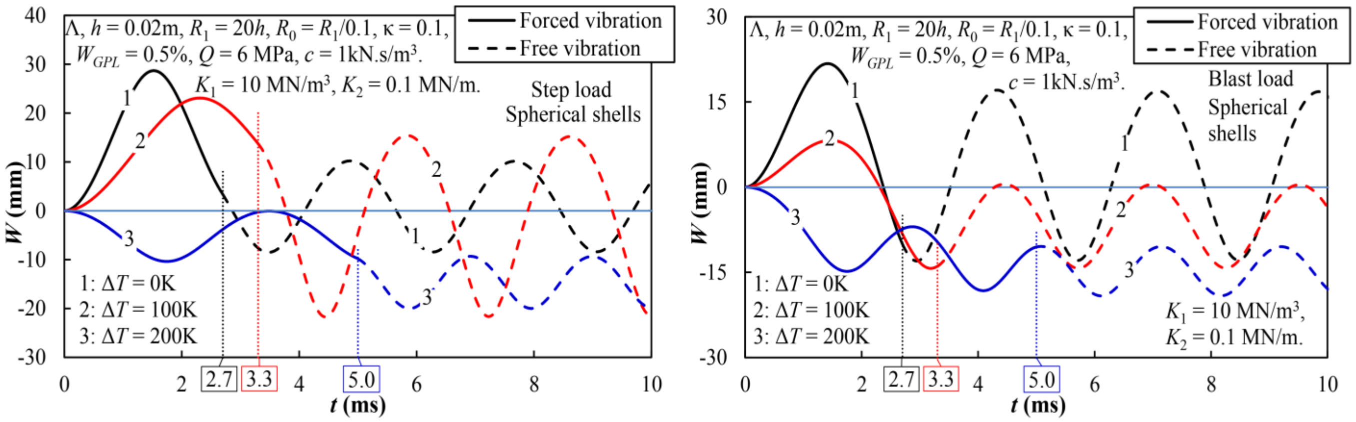

(a) (b)

Fig. 4. Effects of environmental temperatures on the dynamic responses of FG-GPLRC spherical caps under impulse loads

Fig. 5 illustrates the influence of damping coefficients and elastic foundation parameters on the nonlinear dynamic responses of FG-GPLRC spherical caps subjected to step and blast impulse loads. The first row (Figs. 5a and 5b) shows the effect of viscous damping, while the second row (Figs. 5c and 5d) examines the influence of the Winkler and Pasternak foundation stiffnesses. In Figs. 5a and 5b, it is observed that increasing the damping coefficient significantly reduces the vibration amplitude in both step and blast load cases. The suppressing effect of damping becomes more pronounced after the impulse load has ceased, particularly under blast excitation (Fig. 5b), where the system exhibits stronger transient oscillations. Figs. 5c and 5d explore the effects of increasing the foundation stiffness parameters. Both Winkler and Pasternak components contribute to the overall stiffness of the foundation-structure interaction system. As these parameters increase, the dynamic deflection of the spherical cap decreases substantially. It can be explained that the presence of the Pasternak shear layer provides additional lateral restraint, making the structure less susceptible to deformation under radial impulse loads.

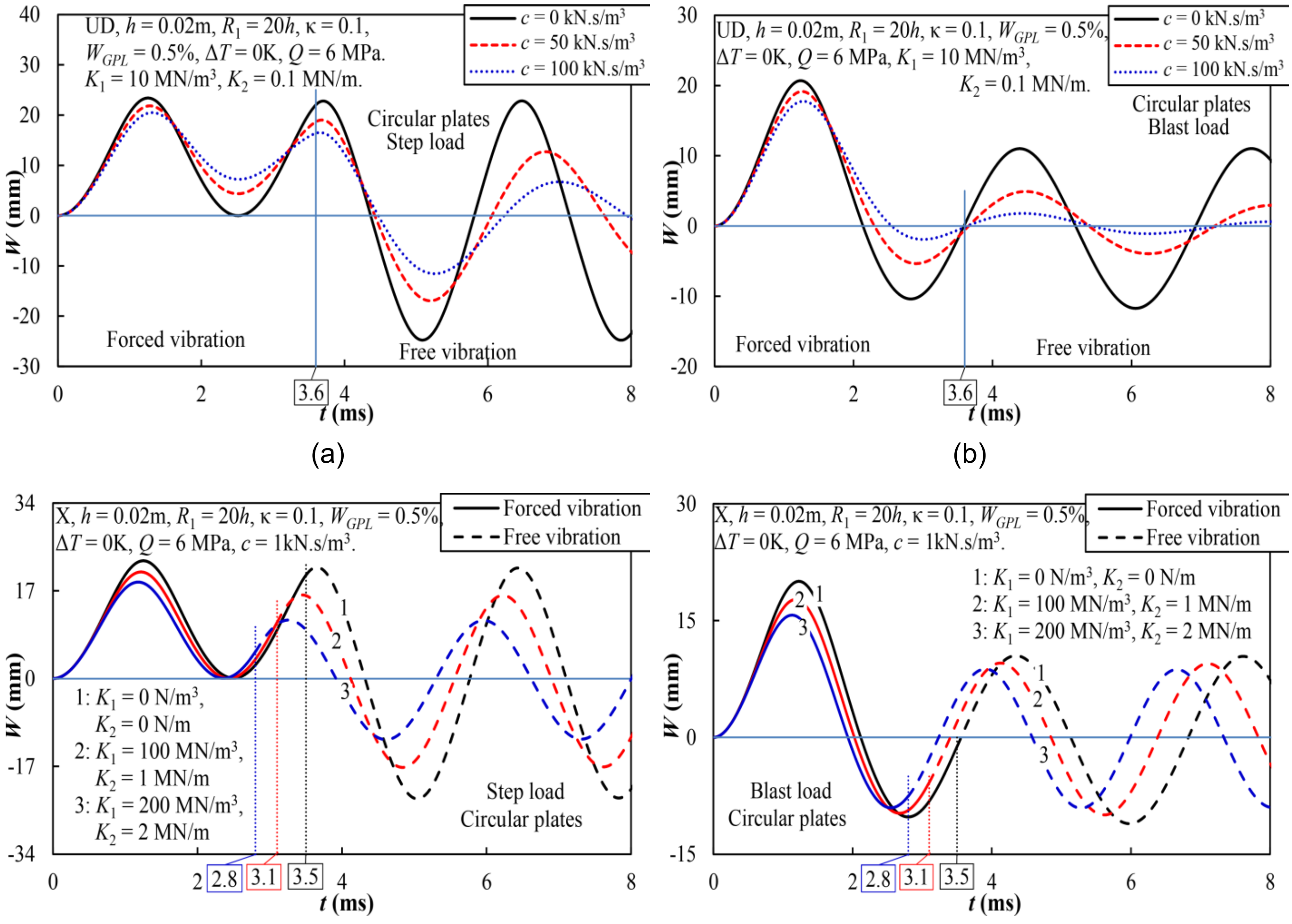

(a) (b)

(c) (d)

Fig. 5. Effects of damping coefficients and foundation parameters on the dynamic responses of FG-GPLRC spherical caps under impulse loads

5. Conclusion

This study has developed a semi-analytical approach for analyzing the nonlinear dynamic responses of FG-GPLRC shallow spherical caps under impulse loads, including step and blast pressure, in a thermally affected environment. The formulation is based on higher-order shear deformation theory (HSDT) incorporating von Karman geometric nonlinearity, and considers the interaction with a nonlinear viscoelastic Pasternak-type foundation. The governing equations are derived using the Lagrangian and Rayleigh dissipation function principles, and solved numerically via the Runge-Kutta method. Extensive parametric studies were carried out to investigate the influence of GPL distribution types, GPL mass fraction, geometrical characteristics, temperature-induced initial deformation, damping coefficients, and foundation stiffness parameters on the dynamic behavior of FG-GPLRC spherical caps and circular plates. The results revealed several key insights:

The X-type GPL distribution, which places reinforcement near the outer surfaces, provides the highest structural stiffness and lowest dynamic deflection under impulse loads.

Increasing the GPL mass fraction leads to enhanced bending rigidity and reduced vibration amplitudes.

Geometric curvature and base radius significantly affect the dynamic response, with deeper and smaller-radius caps exhibiting higher stiffness.

Although material properties are assumed to be temperature-independent, thermal expansion induces pre-deflections that shift the oscillation response domain.

Damping and foundation stiffness (both Winkler and Pasternak components) effectively mitigate dynamic amplitudes, particularly in post-loading stages.

Declaration of conflicting interests:

The author(s) declared no potential conflicts of interest with respect to the research, authorship, and/or publication of this article.

References

[1] J.N. Reddy, E. Ruocco, J.A. Loya, A.M.A. Neves. (2021). Theories and analyses of functionally graded circular plates. *Composites Part C: Open Access*, 5, 100166. https://doi.org/10.1016/j.jcomc.2021.100166

[2] M.M. Ghomshei. (2020). A numerical study on the thermal buckling of variable thickness Mindlin circular FGM plate on a two-parameter foundation. *Mechanics Research Communications*, 108, 103577. https://doi.org/10.1016/j.mechrescom.2020.103577

[3] M. Shariyat, M.M. Alipour. (2013). Semi-analytical consistent zigzag-elasticity formulations with implicit layerwise shear correction factors for dynamic stress analysis of sandwich circular plates with FGM layers. *Composites Part B: Engineering*, 49, 43-64. https://doi.org/10.1016/j.compositesb.2013.01.001

[4] Y. Kiani. (2017). Axisymmetric static and dynamics snap-through phenomena in a thermally postbuckled temperature-dependent FGM circular plate. *International Journal of Non-Linear Mechanics*, 89, 1-13. https://doi.org/10.1016/j.ijnonlinmec.2016.11.003

[5] R. Lal, R. Saini. (2020). Vibration analysis of FGM circular plates under non-linear temperature variation using generalized differential quadrature rule. *Applied Acoustics*, 158, 107027. https://doi.org/10.1016/j.apacoust.2019.107027

[6] C. Chu, M.S.H. Al-Furjan, R. Kolahchi, A. Farrokhian. (2023). A nonlinear Chebyshev-based collocation technique to frequency analysis of thermally pre/post-buckled third-order circular sandwich plates. *Communications in Nonlinear Science and Numerical Simulation*, 118, 107056. https://doi.org/10.1016/j.cnsns.2022.107056

[7] R. Shahsiah, M.R. Eslami, R. Naj. (2006). Thermal instability of functionally graded shallow spherical shell. *Journal of Thermal Stresses*, 29(8), 771-790. https://doi.org/10.1080/01495730600705406

[8] M.S. Boroujerdy, M.R. Eslami. (2014). Thermal buckling of piezoelectric functionally graded material deep spherical shells. *The Journal of Strain Analysis for Engineering Design*, 49(1), 51-62. https://doi.org/10.1177/0309324713484905

[9] L.N. Ly, D.T.N. Thu, D.T. Dong, V.M. Duc, B.T. Tu, N.T. Phuong, V.H. Nam. (2023). A Novel Analytical Approach for Nonlinear Thermo-Mechanical Buckling of Higher-Order Shear Deformable Porous Circular Plates and Spherical Caps with FGM Face Sheets. *International Journal of Applied Mechanics*, 15(05), 2350035. https://doi.org/10.1142/S1758825123500357

[10] S. Qiao, X. Shang, E. Pan. (2016). Characteristics of elastic waves in FGM spherical shells, an analytical solution. *Wave Motion*, 62, 114-128. https://doi.org/10.1016/j.wavemoti.2016.01.001

[11] J. Xie, X. Gou, P. Shi. (2025). Exact solutions for the linear hardening elastoplastic model in functionally graded spherical shell. *Composite Structures*, 366, 119208. https://doi.org/10.1016/j.compstruct.2025.119208

[12] J. Cao, H. Li, Z. Qin, Y. Liu, H. Zhang, X. Wang, Q. Han. (2025). Multi-objective optimization for vibration suppression and weight reduction in composite sandwich shallow-spherical shells with functionally graded coating. *Mechanical Systems and Signal Processing*, 236, 113049. https://doi.org/10.1016/j.ymssp.2025.113049

[13] T. Huang, K. Zhu, Q. Wang, R. Zhong. (2025). Dynamic analysis of prestressed laminated stepped spherical-cylindrical shells. *Advances in Engineering Software*, 210, 104018.https://doi.org/10.1016/j.advengsoft.2025.104018

[14] R. Gholami, R. Ansari. (2017). Large deflection geometrically nonlinear analysis of functionally graded multilayer graphene platelet-reinforced polymer composite rectangular plates. *Composite Structures*, 180, 760-771. https://doi.org/10.1016/j.compstruct.2017.08.053

[15] R. Gholami, R. Ansari. (2019). Nonlinear stability and vibration of pre/post-buckled multilayer FG-GPLRPC rectangular plates. *Applied Mathematical Modelling*, 65, 627-660.https://doi.org/10.1016/j.apm.2018.08.038

[16] R. Ansari, R. Hassani, R. Gholami, H. Rouhi. (2021). Buckling and Postbuckling of Plates Made of FG-GPL-Reinforced Porous Nanocomposite with Various Shapes and Boundary Conditions. *International Journal of Structural Stability and Dynamics*, 21(05), 2150063.https://doi.org/10.1142/S0219455421500632

[17] Y. Kiani, K.K. Żur. (2022). Free vibrations of graphene platelet reinforced composite skew plates resting on point supports. *Thin-Walled Structures*, 176, 109363. https://doi.org/10.1016/j.tws.2022.109363

[18] Y. Liu, Y. Chen, C. Shao, A.M. Alshamrani. (2024). The efficient data-driven solution to estimate the nonlinear bending of sandwich doubly curved panel subjected to transient loading. *Aerospace Science and Technology*, 147, 108980. https://doi.org/10.1016/j.ast.2024.108980

[19] Y. Heydarpour, M. Mohammadzaheri, M. Ghodsi, P. Soltani, F. AlJahwari, I. Bahadur, B. Al-Amri. (2020). Application of the hybrid DQ-Heaviside-NURBS method for dynamic analysis of FG-GPLRC cylindrical shells subjected to impulse load. *Thin-Walled Structures*, 155, 106914. https://doi.org/10.1016/j.tws.2020.106914

[20] S.W. Yang, Y.X. Hao, W. Zhang, L. Yang, L.T. Liu. (2021). Free vibration and buckling of eccentric rotating FG-GPLRC cylindrical shell using first-order shear deformation theory. *Composite Structures*, 263, 113728. https://doi.org/10.1016/j.compstruct.2021.113728

[21] X. Huang, J. Yang, Z. Yang. (2021). Thermo-elastic analysis of functionally graded graphene nanoplatelets (GPLs) reinforced closed cylindrical shells. *Applied Mathematical Modelling*, 97, 754-770.https://doi.org/10.1016/j.apm.2021.04.027

[22] M. Javani, Y. Kiani, M. R. Eslami. (2020). Thermal buckling of FG graphene platelet reinforced composite annular sector plates. *Thin-Walled Structures*, 148, 106589.https://doi.org/10.1016/j.tws.2019.106589

[23] Y. Wang, R. Zeng, M. Safarpour. (2022). Vibration analysis of FG-GPLRC annular plate

in a thermal environment. *Mechanics Based Design of Structures and Machines*, 50(1), 352-370.https://doi.org/10.1080/15397734.2020.1719508

[24] M. Saadatfar, M.H. Zarandi. (2020). Deformations and Stresses of an Exponentially Graded Magneto-Electro-Elastic Non-Uniform Thickness Annular Plate Which Rotates with Variable Angular Speed. *International Journal of Applied Mechanics*, 12(5), 2050050. https://doi.org/10.1142/S1758825120500507

[25] Y.W. Zhang, G.L. She, M.A. Eltaher. (2023). Nonlinear transient response of graphene platelets reinforced metal foams annular plate considering rotating motion and initial geometric imperfection. *Aerospace Science and Technology*, 142(Part B), 108693.https://doi.org/10.1016/j.ast.2023.108693

[26] J.P. Song, G.L. She, M.A. Eltaher. (2024). Nonlinear aero-thermo-elastic flutter analysis of stiffened graphene platelets reinforced metal foams plates with initial geometric imperfection. *Aerospace Science and Technology*, 147, 109050.https://doi.org/10.1016/j.ast.2024.109050

[27] T.H. Chien, P.V. Phuc. (2020). A meshfree approach using naturally stabilized nodal integration for multilayer FG GPLRC complicated plate structures. *Engineering Analysis with Boundary Elements*, 117, 346-358.https://doi.org/10.1016/j.enganabound.2020.04.001

[28] M. Javani, Y. Kiani, M.R. Eslami. (2021). Geometrically nonlinear free vibration of FG-GPLRC circular plate on the nonlinear elastic foundation. *Composite Structures*, 261, 113515.https://doi.org/10.1016/j.compstruct.2020.113515

[29] L.N. Ly, B.T. Tu, D.T.N. Thu, D.T. Dong, V.M. Duc, N.T. Phuong. (2023). Nonlinear thermo-mechanical buckling and postbuckling of sandwich FG-GPLRC spherical caps and circular plates with porous core by using higher-order shear deformation theory. *Journal of Thermoplastic Composite Materials*, 36(10), 4083-4105. https://doi.org/10.1177/08927057221147827

[30] N.T. Phuong, D.T. Dong, B.T. Tu, V.M. Duc, L.N. Khuong, P.T. Hieu, V.H. Nam. (2024). Nonlinear thermo-mechanical axisymmetric stability of FG-GPLRC spherical shells and circular plates resting on nonlinear elastic medium. *Ships and Offshore Structures*, 19(6), 820-830. https://doi.org/10.1080/17445302.2023.2214489

[31] B.T. Tu, L.N. Ly, N.T. Phuong. (2022). A new analytical approach of nonlinear thermal buckling of FG-GPLRC circular plates and shallow spherical caps using the FSDT and Galerkin method. *Vietnam Journal of Mechanics*, 44(4), 418-430. https://doi.org/10.15625/0866-7136/17932

[32] D. Liu, Y. Zhou, J. Zhu. (2021). On the free vibration and bending analysis of functionally graded nanocomposite spherical shells reinforced with graphene nanoplatelets: Three-dimensional elasticity solutions. *Engineering Structures*, 226, 111376. https://doi.org/10.1016/j.engstruct.2020.111376

[33] V.H. Nam, T.Q. Minh, P.T. Hieu, V.T. Hung, B.T. Tu, N.T.T. Hoai, D.T. Dong. (2023). A new analytical approach for nonlinear thermo-mechanical postbuckling of FG-GPLRC circular plates and shallow spherical caps stiffened by spiderweb stiffeners. *Thin-Walled Structures*, 193, 111296. https://doi.org/10.1016/j.tws.2023.111296

[34] V.H. Nam, P.T. Hieu, N.V. Tien, T.Q. Minh, N.T. Phuong. (2025). Nonlinear Thermomechanical Static and Dynamic Buckling Responses of FG-GPLRC Spherical Caps and Circular Plates with Two-Step Spiderweb Stiffeners and a Piezoelectric Layer. *Journal of Engineering Mechanics*, 151(7), 04025028.https://doi.org/10.1061/JENMDT.E

MENG-8363

[35] V.H. Nam, N.T.T. Hoai, N.V. Tien, P.T. Hieu, N.T. Phuong. (2025). Nonlinear thermo-mechanical static and dynamic buckling responses of functionally graded porous graphene-reinforced spherical shells and circular plates with spider-web stiffeners. *Journal of Thermoplastic Composite Materials,* 39(2), 702-732. https://doi.org/10.1177/08927057251355139

[36] V.H. Nam, N.T.T. Hoai, K.Q. Thai, P.T. Hieu, D.T. Dong. (2025). Nonlinear hygro-thermo-mechanical postbuckling of spiderweb-stiffened sandwich FG-GPLRC spherical shells and circular plates with porous core. *Acta Mechanica* 237, 925-947. https://doi.org/10.1007/s00707-025-04542-z